JOURNAL OF MATERIALS SCIENCE **33** (1998) 5759–5771

Analysis of Planar Defects in Nb_2O_5- and Bi_2O_3-doped $BaTiO_3$ Ceramics

MICHAEL A. MCCOY,*‡ WILLIAM E. LEE,* ROBIN W. GRIMES‡
*Department of Engineering Materials, University of Sheffield, Mappin Street, Sheffield, S1 3JD, UK and ‡Department of Materials, Imperial College of Science, Technology and Medicine, London SW7 2BP, UK

ROBERT KEYSE
Department of Materials Science and Engineering, University of Liverpool, Liverpool L69 3BX, UK

The structure and chemistry of planar defects in Nb_2O_5- and Bi_2O_3-doped $BaTiO_3$ ceramics that exhibit "core-shell" microstructures have been examined using a combination of conventional transmission (CTEM) and high-resolution (HREM) and scanning transmission (STEM) electron microscopy and microanalysis. In addition to ferroelectric domain boundaries within the core, twins and "stacking faults" were observed, both with interface planes lying along {1 1 1}. Unlike the twins, stacking faults were observed only within the paraelectric shell region of the $BaTiO_3$ grain; these planar defects are enriched in Nb and Bi relative to the surrounding matrix. The combined CTEM contrast analysis and HREM observations suggest a fault displacement vector normal to the fault plane of magnitude $1/2\langle 1\ 1\ 1\rangle + x\langle 1\ 1\ 1\rangle (x = 0.1)$; a proposed fault structure is based on a double BiO_3^{3-} layer with bismuth cations occupying barium sites and charge compensation by Nb^{5+} substitution in adjacent octahedral sites. In addition, the incorporation mechanism of Nb_2O_5 and Bi_2O_3 into $BaTiO_3$ is discussed with respect to microanalysis results.

1. Introduction

The temperature-stable dielectric response of X7R barium titanate ($BaTiO_3$) dielectrics is based on the formation of a core-shell microstructure [1] in which individual grains contain a ferroelectric core surrounded by a paraelectric shell. The formation of this heterogeneous microstructure is largely dependent on the activity and diffusion of dopants during the sintering process. During sintering of a model X7R based on Nb_2O_5 and Bi_2O_3 doping, the dopants react with the $BaTiO_3$ grains to form a number of intermediate Aurivillius compounds, including $BaBi_4Ti_4O_{15}$, $BaBi_2Nb_2O_9$, Bi_3TiNbO_9, and a tungsten bronze phase $Ba_4Bi_2Ti_4Nb_6O_{30}$, believed to act as the dopant source [2, 3]. The dopants diffuse rapidly along grain boundaries and surfaces of the $BaTiO_3$ grains and slowly diffuse into the grain interior. Depending on the sintering conditions and the starting chemistry, the $BaTiO_3$ grains may exhibit a dopant concentration gradient from the edge of the grain into the core. The final microstructure of a typical commercial X7R capacitor consists of grains with a core region containing a relatively low dopant concentration surrounded by a shell that contains higher dopant levels [4, 5]. The undoped core is ferroelectric, showing characteristic 90° ferroelectric domain boundaries, whereas in the shell, the higher dopant concentration stabilizes the paraelectric phase to room temperature. Since the dopant concentration controls local Curie temperature, the variation of local chemistry within the ceramic causes a distribution in the Curie temperature with a corresponding flat response of dielectric constant with temperature.

In addition to ferroelectric domain boundaries, other planar defects have frequently been observed within the microstructure, consisting either of twin boundaries [6, 7] or stacking faults [1]. In the present study, the structure and chemistry of stacking faults in a model X7R $BaTiO_3$ ceramic, codoped with Nb_2O_5 and Bi_2O_3, have been examined, and a model is proposed for their formation. We also briefly address the point defect chemistry of Nb and Bi incorporation in $BaTiO_3$ with respect to the results of microchemical analyses performed in the present study.

2. Experimental

2.1. Sample preparation

$BaTiO_3$ ceramics containing approximately 4.5 mol% Nb_2O_5 and 4.5 mol% Bi_2O_3 were prepared by mixing reagent grade powders of $BaTiO_3$, Nb_2O_5, and Bi_2O_3. The powders were milled in an aqueous suspension for 15 h, dried and granulated to a granule size $<500\ \mu$m. Pellets 1.0 cm in diameter and approximately 2 mm thick were pressed (at 125 MPa) and sintered for 1 h at

1100 °C; both heating and cooling rates were 10 K/min. The pellets were wrapped in Pt foil during sintering to minimize bismuth volatilization. Both the dopant concentration and sintering schedule were chosen to optimize densification with a minimum of bismuth loss and have previously been shown to produce microstructures with well-defined core-shell behaviour [1].

Specimen preparation for transmission electron microscopy (TEM) analysis followed conventional procedures, including ultrasonic cutting a 3-mm diameter disc, followed by grinding and lapping to a sample thickness <80 μm. The center of the sample was further thinned mechanically to a final thickness of <10 μm using a dimpler and ion milled at 5 kV to electron transparency using a Gatan Duomill. A steel specimen platform was used for the ion-milling operation, since surface contamination from conventional molybdenum holders would mask X-ray signals arising from Nb and Bi.

2.2. STEM energy-dispersive X-ray spectroscopy microanalysis

Energy-dispersive X-ray spectroscopy (EDS) was performed using an VG-601UX dedicated STEM, operated at 100 kV, and a windowless Si(Li) detector. Both individual spectra as well as X-ray line scans were used to determine the chemistry of the planar defects and the surrounding matrix. Quantification of the spectral data was performed by a curve-fitting standardless method using the RTS-2 quantification package. The Cliff-Lorimer k factors used in the analysis were based on a combination of experimentally fitted detector parameters and previous examination of X-ray peak profiles of test materials with known chemical composition. The main difficulty in EDS analysis of $BaTiO_3$ is the overlap of Ba-L and Ti-K X-ray peaks; because of the X-ray peak overlap, the direct analysis of the amount of Ba and Ti is particularly sensitive to the parameters used in the quantification. Relative changes in the Ba : Ti ratio, however, could be ascertained by examining the ratio of the Ba Lγ at *ca.* 5.53–5.79 keV (which contains no Ti contribution) and comparing the integrated peak intensity to the Ba Lα-Ti Kα (*ca.* 4.46–4.51 keV) and Ba Lβ-Ti Kβ (*ca.* 4.83–4.93 keV) intensities to establish a Ba + Ti : Ba ratio.

The EDS line scans measured the relative integrated X-ray intensities for selected energy windows as a function of specimen position as the electron probe was scanned across the (stacking fault) interface. The windows were constructed for the following X-ray peak intensities: (1) Ba-Lγ1, (2) Ba-Lγ2, (3) Ba-Lα and Ti-Kα, (4) Bi-Lα, (5) Bi-Lγ, (6) Bi-M, (7) Nb-Kα, and (8) Nb-L. The data for windows corresponding to a particular element were combined to improve the signal-to-noise statistics. A total of 32 points were sampled along a line scan length of 28 nm. The effective probe size is estimated to be on the order of 1 nm.

2.3. CTEM and HREM analysis methodology

Samples were analysed using both CTEM (JEOL 200 CX operating at 200 kV) and HREM (JEOL 3010 operating at 300 kV). The CTEM experiments were performed to determine the interface plane and to provide information about the fault displacement vector **R**. The displacement vector can be determined by a fault contrast analysis in which the diffraction contrast of an inclined fault is observed under a variety of two-beam imaging conditions [8]. For a stacking fault, contrast extinctions occur when the phase angle $\alpha = 2\pi \mathbf{g} \cdot \mathbf{R} = 2\pi n (n = \text{integer})$, where **g** is the operating reflection. A detailed review of the methodology is provided by Amelinckx [9].

The HREM experiments examined the stacking faults in ⟨1 1 0⟩ projection. For each region, a series of images at well-defined defocus steps was recorded. Image simulation was performed using a multislice code in the EMS V3.30 software package developed by Stadelmann [10]. A structural model of the (1 1 1) fault boundary was built into an orthogonal supercell with dimensions a, b, and c along the respective [1 1 1], [2 $\bar{1}$ 1], and [0 $\bar{1}$ 1] directions of the original cubic perovskite unit cell. The interface plane was placed in the middle of the supercell and simulated HREM images were calculated with the c direction of the supercell parallel to the incident electron beam using the appropriate microscope and specimen parameters. The dimension along the [1 1 1] direction was adjusted to avoid any artefacts in the simulated image arising from the supercell boundary. Electron-optical parameters such as beam convergence and aperture size were measured from diffraction patterns. A through-focal series of images was calculated, and the defocus and specimen thickness were determined by matching simulated images of the perovskite structure matrix with the HREM micrographs.

3. Results and discussion

3.1. CTEM analysis

Fig. 1 shows typical microstructures, consisting of $BaTiO_3$ grains containing a ferroelectric core whose contrast is dominated by ferroelectric domain boundaries surrounded by a paraelectric shell. In addition to the ferroelectric domain boundaries, two types of planar defects were commonly observed within these $BaTiO_3$ grains: twin boundaries (Fig. 1a) and stacking faults (Fig. 1b). The twin boundaries bisected the $BaTiO_3$ grains, crossing through both the paraelectric shell and the ferroelectric core; the stacking faults, however, were observed exclusively within the shell region. The faults often intersected other faults, and some also terminated within the grain via formation of a dislocation at the fault edge. A trace analysis using CTEM showed that both the twins (Fig. 2) and stacking faults lie along {1 1 1} planes.

Contrast analysis experiments were performed on six different stacking faults in a single $BaTiO_3$ grain. The results of the $\mathbf{g} \cdot \mathbf{R}$ contrast analysis experiments are shown in Table I. The displacement vectors, as determined by fault contrast "invisibility criteria," lie normal to the interface plane along ⟨1 1 1⟩; this observation was consistent with a previous study [1], as well as with direct measurements made from HREM micrographs.

TABLE I CTEM fault contrast analysis

	Operating reflection					
	$\mathbf{g}_{121}$	$\mathbf{g}_{12\bar{1}}$	$\mathbf{g}_{100}$	$\mathbf{g}_{1\bar{1}0}$	$\mathbf{g}_{110}$	$\mathbf{g}_{011}$
Fault						
A	vis	vis	vis	vis	inv	vis
B	vis	vis	vis	vis	inv	vis
C	vis	vis	vis	vis	inv	vis
D	vis	vis	vis	inv	vis	vis
E	vis	inv	vis	inv	vis	inv
F	vis	inv	vis	inv	vis	inv

inv = no fault contrast
vis = visible fault contrast

3.2. HREM analysis of stacking faults

Fig. 3 shows a stacking fault viewed edge-on ($\langle 1\,1\,0\rangle$ projection) taken near Scherzer defocus; the change in the stacking sequence across the boundary can be seen by noting the discontinuity in the stacking of the Ba–O columns that appear as white dots in the micrograph. The HREM experiments confirmed the $\{1\,1\,1\}$ interface plane and measurements made from the micrographs confirmed the $\langle 1\,1\,1\rangle$ displacement vector calculated from the CTEM analysis. Three such faults were analysed and produced similar image contrast. A detailed measurement across the boundary showed that the magnitude of the displacement vector is $1/2\langle 1\,1\,1\rangle$ plus a rigid body translation of approximately $0.1\langle 1\,1\,1\rangle$ (0.07 nm). In addition to the discontinuity across the interface, the images are characterized by a high level of noise at the interface consistent with a high degree of disorder along the fault. Details regarding HREM image simulation of the stacking fault structural models are presented in section 3.4.

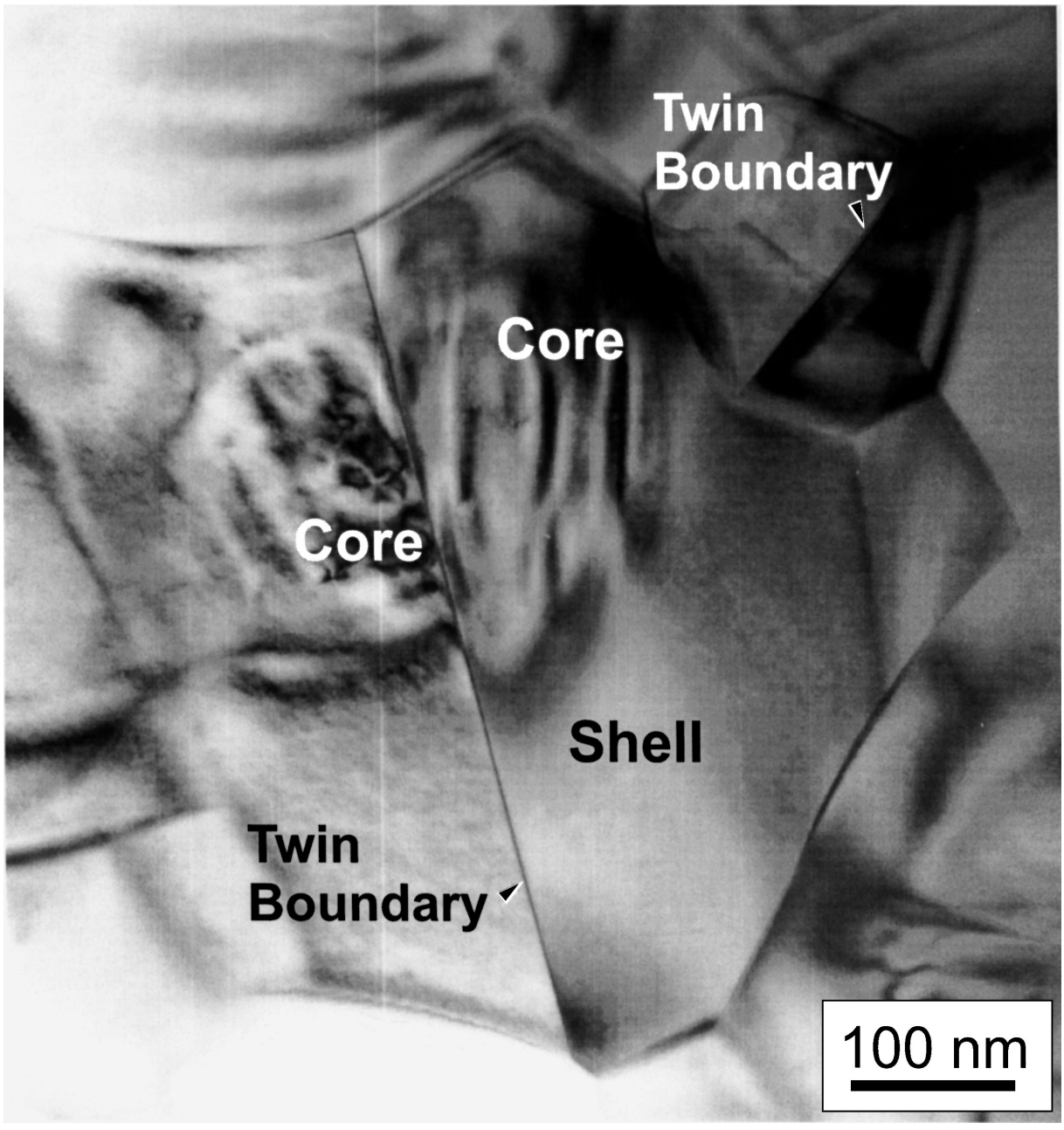

(a)

Figure 1 Bright-field TEM of core-shell microstructure showing (a) twin boundaries and (b) stacking faults within shell. The twins are continuous through both the core and the shell regions in the $BaTiO_3$ grain.

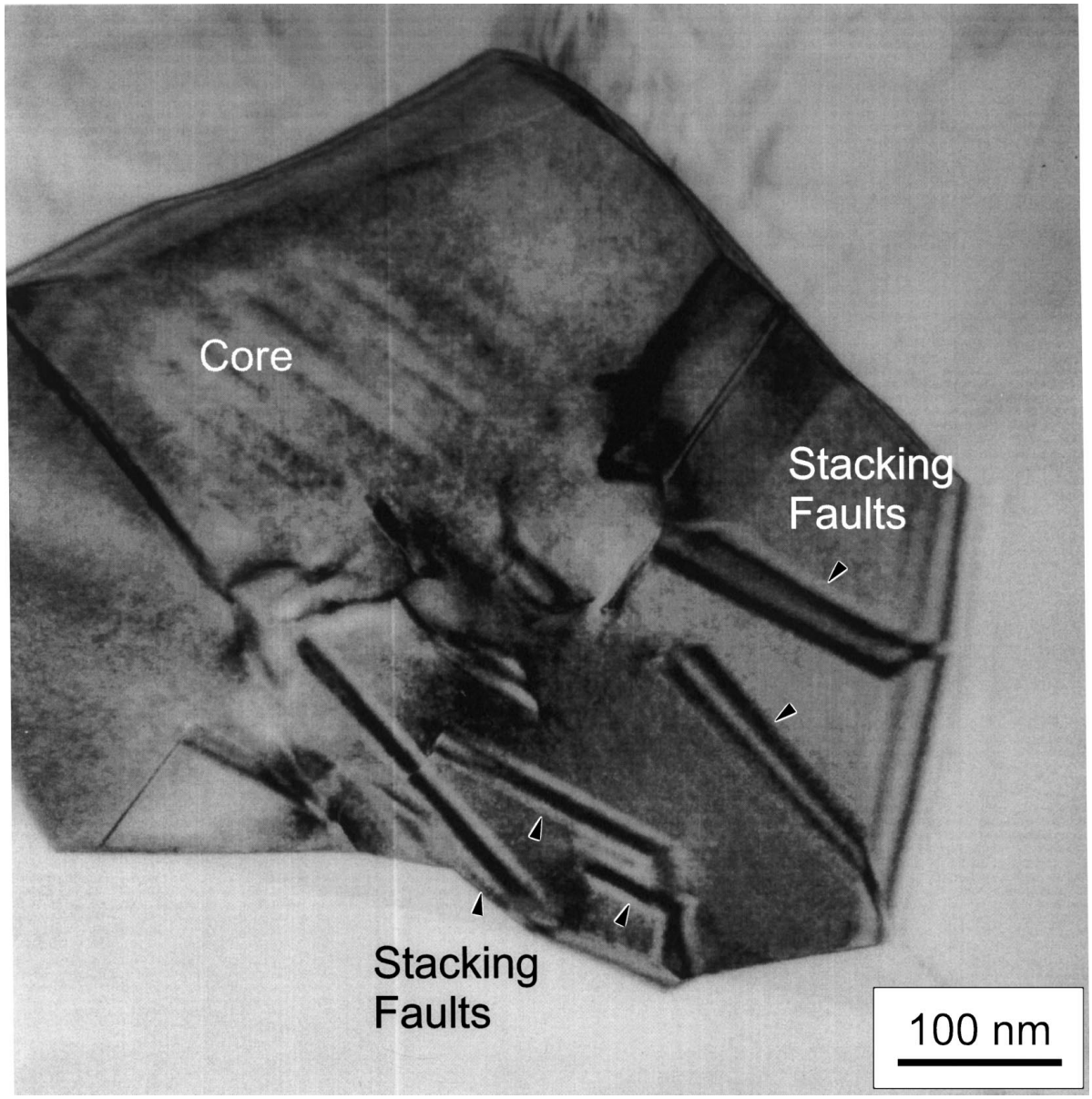

(b)

Figure 1 (*continued*).

3.3. STEM (EDS) microchemical analysis

EDS spectra taken from core and shell regions (Fig. 4) confirmed the presence of a gradient in dopant concentration from the shell region into the core. The average calculated dopant concentration within the shell region (Table II) was *ca.* 2.3 atom % Bi and 2.8 atom % Nb, whereas within the core a lower Bi (*ca.* 1.1 atom %) and Nb ($\leq$0.6 atom %) concentration was detected. The error in the quantification, resulting from a combination of analysis procedures and counting statistics, is $\pm$2 atom % for Ba and Ti and $\pm$0.5 atom % for Bi and Nb.

TABLE II EDS analysis of Nb_2O_5-, Bi_2O_3-$BaTiO_3$: Core/shell microstructures

	Atom %*			
	Bi	Nb	Ba	Ti
Shell	2.3	2.8	50.3	44.6
Core	1.1	0.6	50.5	47.8

*Calculated error is $\pm$2 atom % for Ba and Ti and $\pm$0.5 atom % for Nb and Bi, respectively.

It is interesting to note that the Ba : Ti ratio measured in the EDS analysis was a function of the dopant concentration. Although the Ba concentration remained essentially constant at *ca.* 50 atom %, the calculated Ti concentration decreased as both Nb and Bi concentration increased. Because of the problems caused by Ba-L and Ti-K peak overlap, the absolute value of the Ba : Ti ratio is particularly sensitive to the energy scale calibration. Relative changes in the Ba : Ti ratio are much less susceptible to such effects, however, and the observed changes are certainly consistent with the incorporation of Bi and Nb as point defects on the Ti sublattice of the $BaTiO_3$ structure.

Compositional analysis of stacking faults within the shell revealed much higher dopant concentrations compared with the matrix immediately adjacent to the fault (Fig. 5); the results of quantitative analysis from five different regions (Table III) consistently show a higher

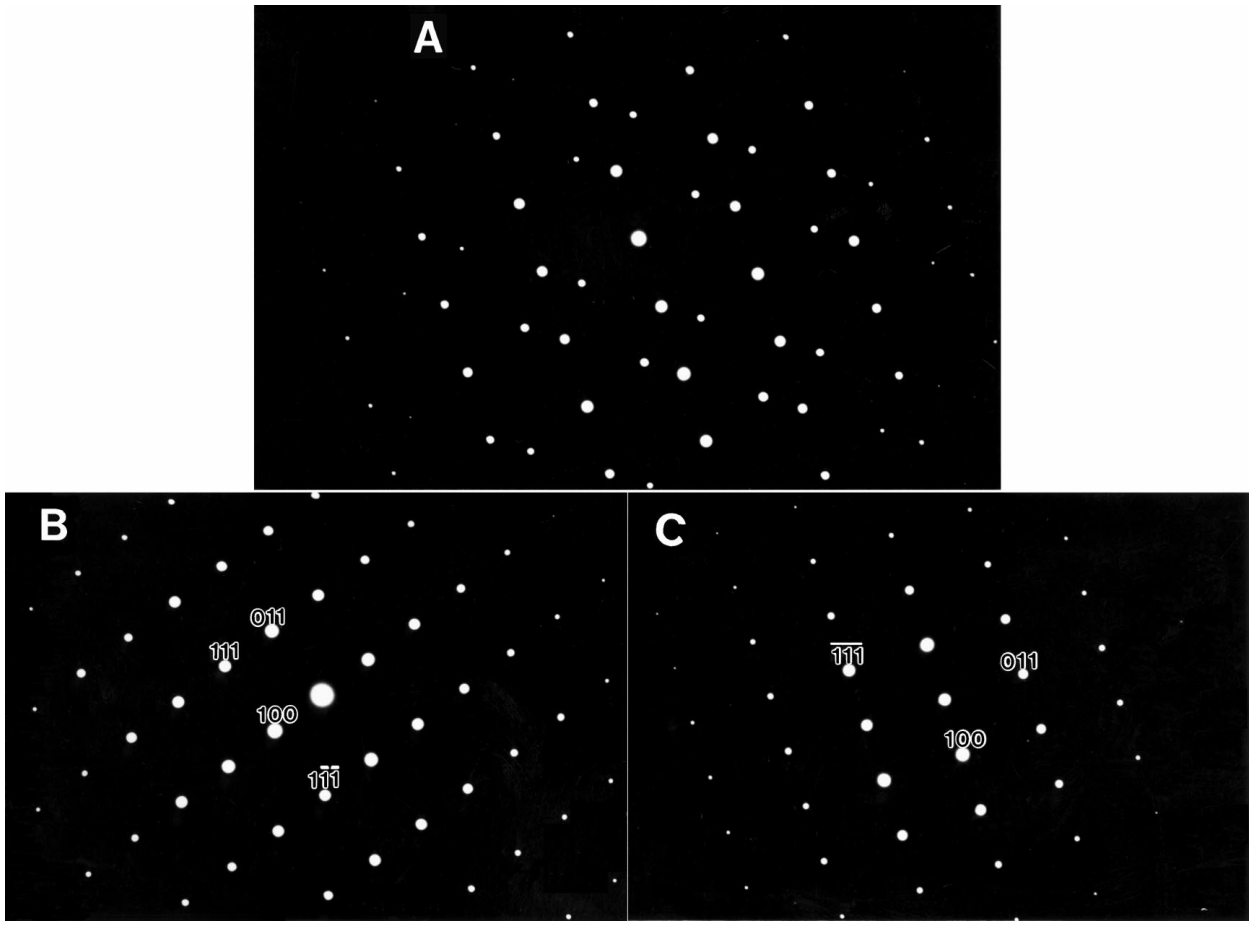

Figure 2 Selected-area electron diffraction patterns ([0 $\bar{1}$ 1] zone axis) of $BaTiO_3$ twins shown in Fig. 1 taken from (A) twin boundary, (B) twin variant to left of boundary, and (C) twin variant to right of boundary. The twin plane is (1 1 1).

level of both Nb (*ca.* 3.9%) and Bi (*ca.* 3.6%). Whereas the variation of the matrix compositions from the different regions may be due in part to general composition differences (*i.e.*, concentration gradients from the grain boundary into the bulk of the grain) inherent in the heterogeneous core-shell microstructure, the consistent differences in Nb and Bi compositions between the fault and matrix suggest enhanced dopant segregation along the stacking fault. This is confirmed by EDS line scans (Fig. 6), which show an abrupt change in composition over a range of 2.5 nm with an increase in Nb and Bi signals and a slight decrease in the (Ba + Ti/Ba) signal. The measured width of the segregation layer is expected to be an overestimation of the real width because of the finite electron probe size and any specimen drift during the line scan. No dopant concentration gradients were observed in the matrix in the vicinity of the fault.

As in the core and shell microanalysis results, the change in Bi and Nb concentration in the stacking fault also changes the Ba : Ti ratio; the Ba concentration was again essentially constant at *ca.* 50 atom %, whereas the calculated Ti concentration decreased with increasing Nb and Bi concentration.

TABLE III EDS analysis of Nb_2O_5-, Bi_2O_3-$BaTiO_3$ comparison of stacking fault and surrounding $BaTiO_3$

	Atom %*			
	Bi	Nb	Ba	Ti
Matrix				
1	2.4	2.9	48.4	46.3
2	2.0	2.2	50.6	45.2
3	2.5	3.0	51.1	43.4
4	2.3	3.2	52.1	42.4
5	2.1	2.5	51.0	44.4
Mean (matrix)	2.3 ± 0.5	2.9 ± 0.5	50.3 ± 2	44.5 ± 2
Stacking Fault				
1	3.0	3.5	48.2	45.3
2	3.5	4.0	51.6	40.9
3	3.7	4.6	49.4	42.3
4	4.9	3.9	47.3	43.9
5	2.9	3.6	48.4	45.1
Mean (fault)	3.6 ± 0.5	3.9 ± 0.5	49.0 ± 2	43.5 ± 2

*Calculated error is ±2 atom % for Ba and Ti and ±0.5 atom % for Nb and Bi, respectively.

3.4. Proposed model for shell stacking fault structure

3.4.1. Description of perfect perovskite structure

The stacking sequence along [1 1 1] for the unfaulted $BaTiO_3$ perovskite structure consists of alternating layers of BaO_3^{4-} and Ti^{4+} separated by 1/6[1 1 1] (0.115 nm). Cations on each layer are displaced from those below by 1/2[1 $\bar{1}$ 1], which is the equivalent of an interplanar translation (1/6[1 1 1]) and an in-plane shear of 1/3[1 $\bar{2}$ 1]. This is shown in the schematic [0 $\bar{1}$ 1] projection of Fig. 7.

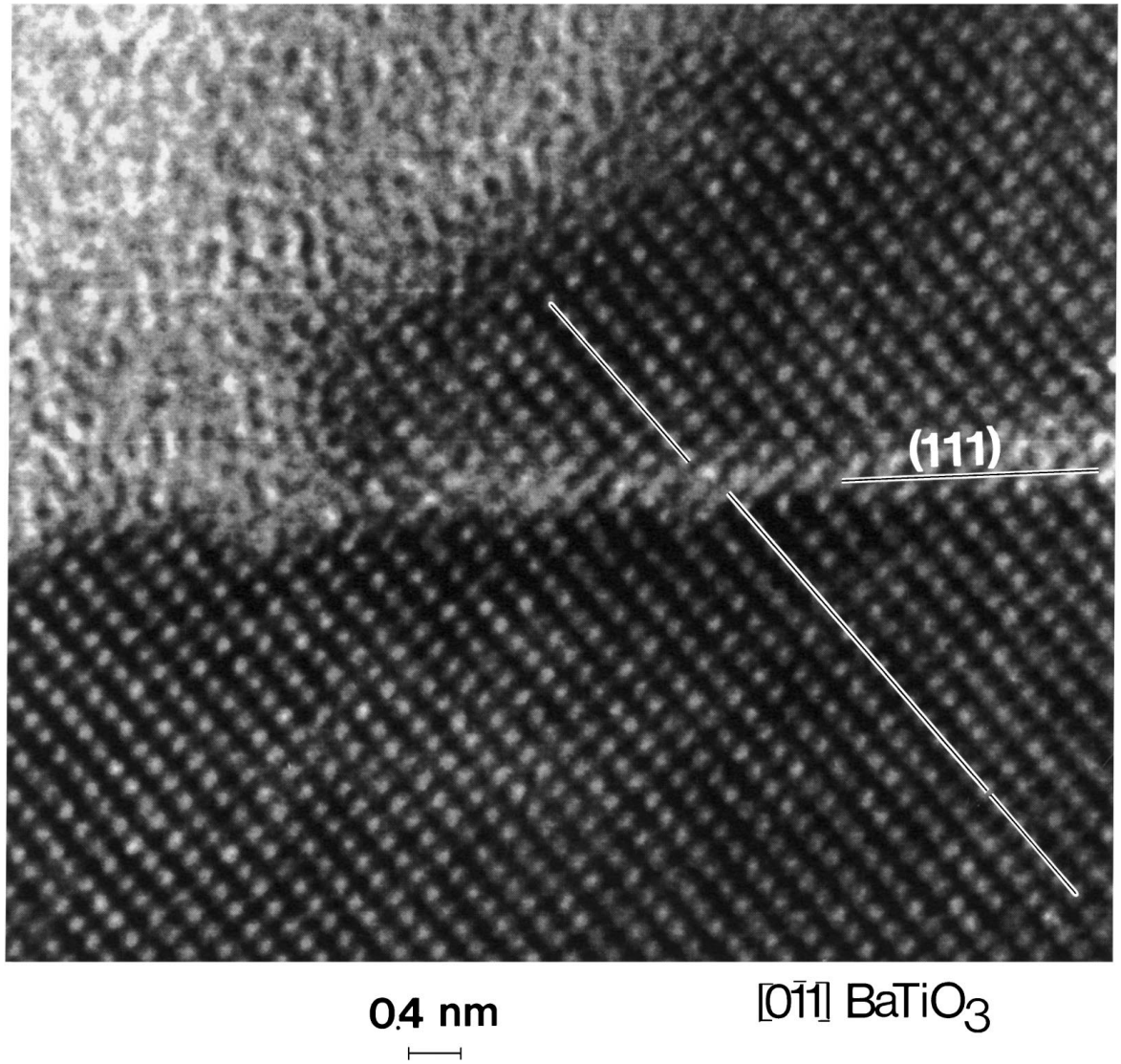

Figure 3 HREM micrograph (near Scherzer defocus) of shell region in ⟨1 1 0⟩ projection showing a stacking fault viewed edge-on. Under these imaging conditions, the white dots correspond to the Ba–O columns. The discontinuity in the Ba–O planes across the boundary can be seen.

In our nomenclature, BaO_3^{4-} and Ti^{4+} layers are represented by uppercase and lowercase letters, respectively. The origin is at a Ba^{2+} ion position, labelled A, and the cation positions A, B, and C correspond to in-plane translations from the origin of 0, $1/3[1\,\bar{2}\,1]$, and $2/3[1\,\bar{2}\,1]$, respectively. The stacking sequence for a perfect crystal is given by

$$\ldots \text{AbCaBc}\{\text{AbCaBc}\}\text{AbCaBc}\ldots$$

The repeat unit, shown by the braces, corresponds to the [1 1 1] repeat (0.692 nm in paraelectric $BaTiO_3$).

3.4.2. Possible stacking fault structures

There are several possible ways of forming a (1 1 1) stacking fault in the perovskite structure. The simplest way involves a shear of $1/3[1\,\bar{2}\,1]$ (*i.e.*, C to A, A to B, B to C), giving

$$\ldots \text{AbCaBcAbC}\mathbf{b}\text{CaBcAcBa}\ldots \qquad (1)$$

The interface plane is shown in boldface. The resulting structure is equivalent to an extra BaO_3^{4-}/Ti^{4+} [Cb] layer, or $\mathbf{R} = 1/3[1\ 1\ 1]$. Note that a shear in the opposite direction ($-1/3[\bar{2}\ 1\ 1]$) (*i.e.*, C to B, A to C, B to A) produces

$$\ldots \text{AbCaBcAbCb}\mathbf{B}\text{cAbCaBc}\ldots \qquad (2)$$

and that by placing a Ba^{2+} (B) directly over a Ti^{4+} (b) position, the local electrostatic (cation) repulsion increases creating an energetically unfavourable situation.

Stacking faults may be also be introduced by either inserting or removing a single layer (BaO_3^{4-} or Ti^{4+}). These structures may either be Ti rich

(a) Ti rich (extra Ti layer)

$$\ldots \text{AbCaBcAb}\mathbf{a}\text{CaBcAbCaB}\ldots \qquad (3)$$
$$\mathbf{R} = 1/6[1\,1\,1]$$

(b) Ti rich (removal of $Ba–O_3$ layer)

$$\ldots \text{AbCaBcAb}\mathbf{a}\text{BcAbCaBc}\ldots \qquad (4)$$
$$\mathbf{R} = -1/6[1\,1\,1]$$

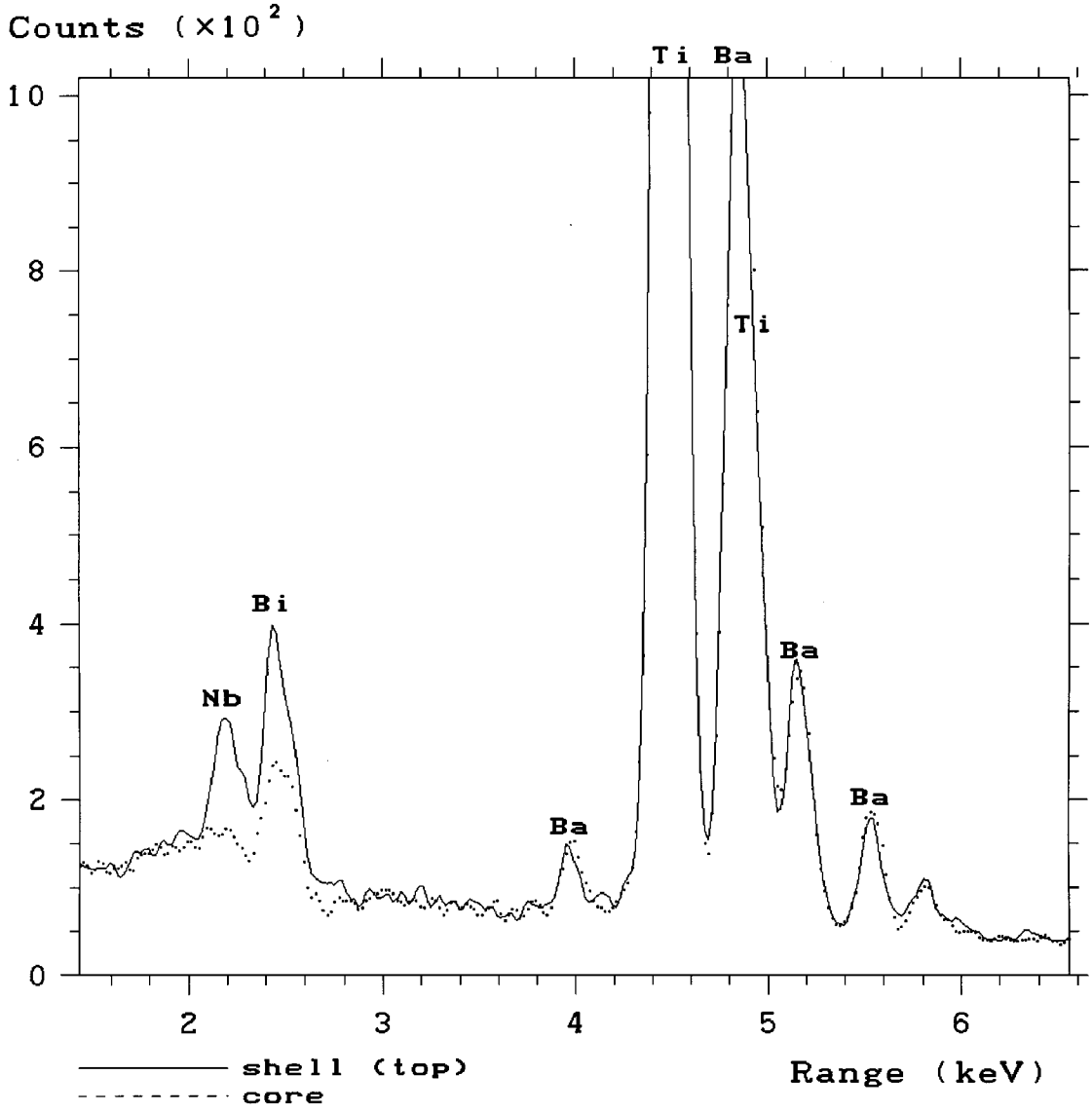

Figure 4 EDS spectra taken from core (dotted line) and shell (solid line) regions within a single $BaTiO_3$ grain. The shell shows significantly higher levels of both Nb and Bi.

or Ba rich

(a) Ba rich (insertion of Ba–O_3) layer

$$\ldots \text{AbCaBcAbC}\mathbf{B}\text{aBcAbCaBc}\ldots \qquad (5)$$

$$\mathbf{R} = 1/6[1\,1\,1]$$

(b) Ba rich (removal of Ti layer)

$$\ldots \text{AbCaBcA}\mathbf{C}\text{aBcAbCaBc}\ldots \qquad (6)$$

$$\mathbf{R} = -1/6[1\,1\,1]$$

Finally, faults may be created with a combination of (1) an insertion or removal of a layer and (2) a shear along $[1\,\bar{2}\,1]$. Only two combinations, either Ti rich

$$\ldots \text{AbCaBc}\mathbf{a}\text{BcAbCaBcAbC}\ldots \qquad (7)$$

$$\mathbf{R} = 1/2[1\,1\,1]$$

or Ba-rich

$$\ldots \text{AbCaBcA}\mathbf{B}\text{cAbCaBcAbC}\ldots \qquad (8)$$

$$\mathbf{R} = 1/2[1\,1\,1],$$

are possible.

Note that the introduction of an extra BaO_3^{4-} or Ti^{4+} layer would violate charge neutrality, requiring the formation of charge-compensating defects (*e.g.*, interstitial oxygen or cation vacancies for Ti-rich layers) to maintain overall charge balance. If the Ba-site cations within the fault consist of trivalent cations with partial occupancy of adjacent Ti sites by Nb^{5+}, however, charge neutrality may be preserved without point defect formation.

3.4.3. Proposed stacking fault model

Several candidates stacking fault structures have been examined, corresponding to Models 1, 5, 6, and 8. Each structural model included the additional rigid-body translation measured from the HREM micrographs of *ca.* $0.1\langle 1\,1\,1\rangle$ (0.07 nm). The best fit, based on the HREM and CTEM analyses, corresponded to Model 8 ($\mathbf{R} = 1/2[1\,1\,1]$).

The proposed model, shown in Fig. 8, incorporates a change in stacking sequence giving rise to a double BaO_3^{4-} interface layer that is proposed to be occupied by bismuth with adjacent Ti sites on either

side of the layer occupied by Nb^{5+}; we assume that the bismuth is in a 3+ oxidation state, since higher oxidation states would cause an effective decrease in the ionic radius [11], thereby destabilizing the dodecahedral co-ordination. The overall formula for the supercell $Ba_{12}Bi_4Ti_{10}Nb_4O_{48}$ is charge neutral. If barium substitutes for any bismuth at the interface, the charge difference may be compensated by the further substitution of Nb^{5+} on Ti^{4+} sites. The structure of the fault differs from that of the Aurivillius type and tungsten bronze precursor phases that have been observed in this system because the defect layers in the Aurivillius structures lie along (0 0 1) planes instead of (1 1 1).

It is useful at this point to discuss the use of the term "stacking fault." Originally, the term was used to describe planar defects in metallic systems in which an atom plane was either added (extrinsic stacking fault) or removed (intrinsic stacking fault). Such planar defects are purely geometric in character, segregation of impurities to such stacking faults was common after their formation but not necessary for them to occur. In ceramic systems, however, the addition of a extra plane will frequently lead to a charge imbalance; for such a defect, charge-compensating defects must be present. These defects, strictly speaking, have both a chemical and a geometrical character.

In the unrelaxed interface structural model, the local environment of the barium (bismuth) sites at the interface is distorted compared with the ideal dodecahedral environment within the perovskite structure. By introducing a relaxation in the cation position of *ca.* 0.05 nm, however, the bond lengths approximate those of the bismuth positions in the Aurivillius phase $Bi_4Ti_3O_{12}$ [12]. Comparison of the respective bond lengths in the refined structural model and the prototype structures is shown in Table IV. A comparison of simulated HREM images based on the refined structural model with the experimental HREM micrograph is shown in Fig. 9. There is, however, a high level of noise and residual contrast within the interface region in the micrograph that is unaccounted for in the simulations. This suggests a high level of local disorder, possibly due to local site relaxation.

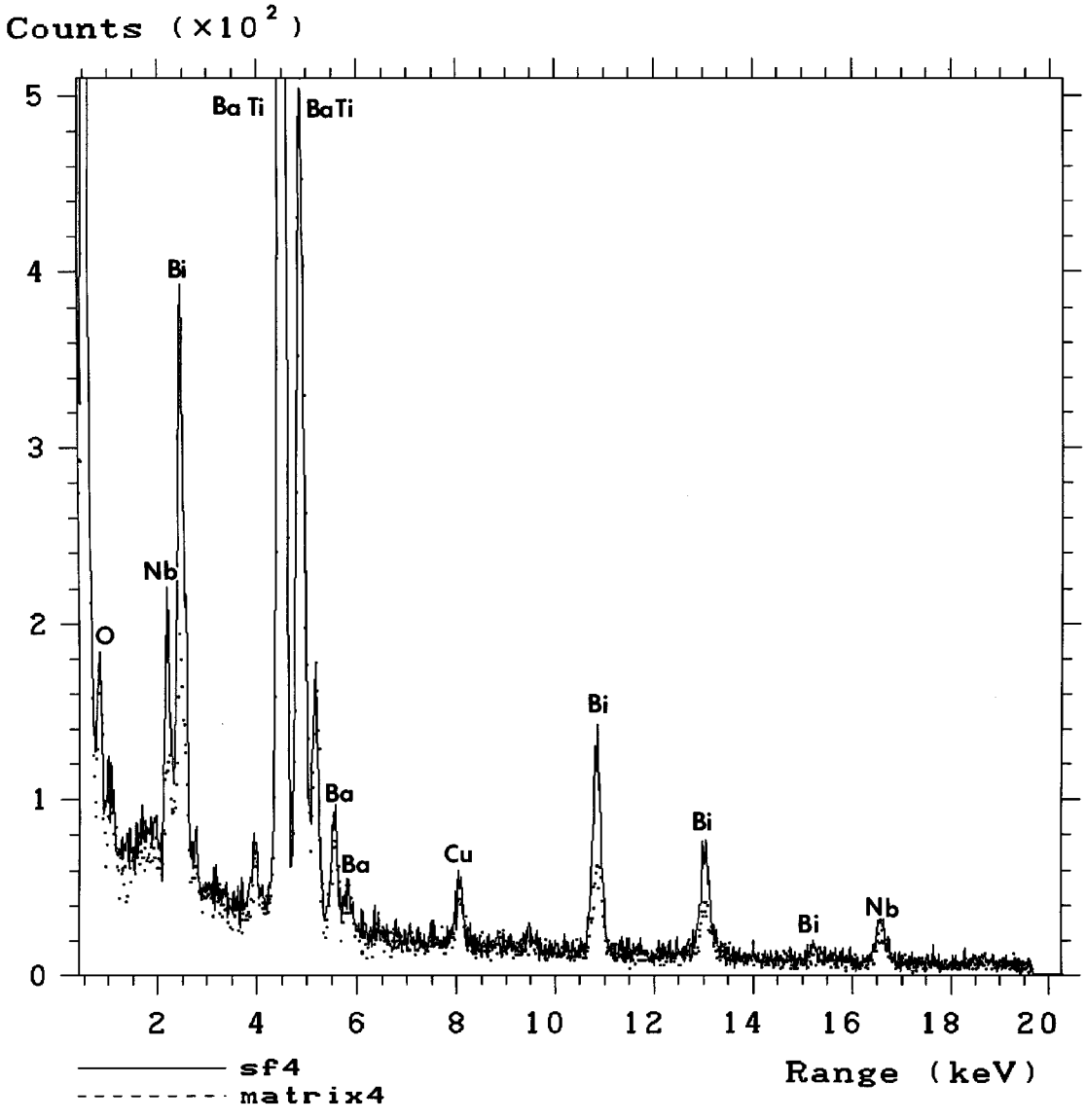

(a)

Figure 5 (a, b) EDS spectra taken from stacking fault (solid line) and matrix (dotted line) immediately adjacent to fault. Significantly higher levels of both Nb and Bi are observed within the stacking fault.

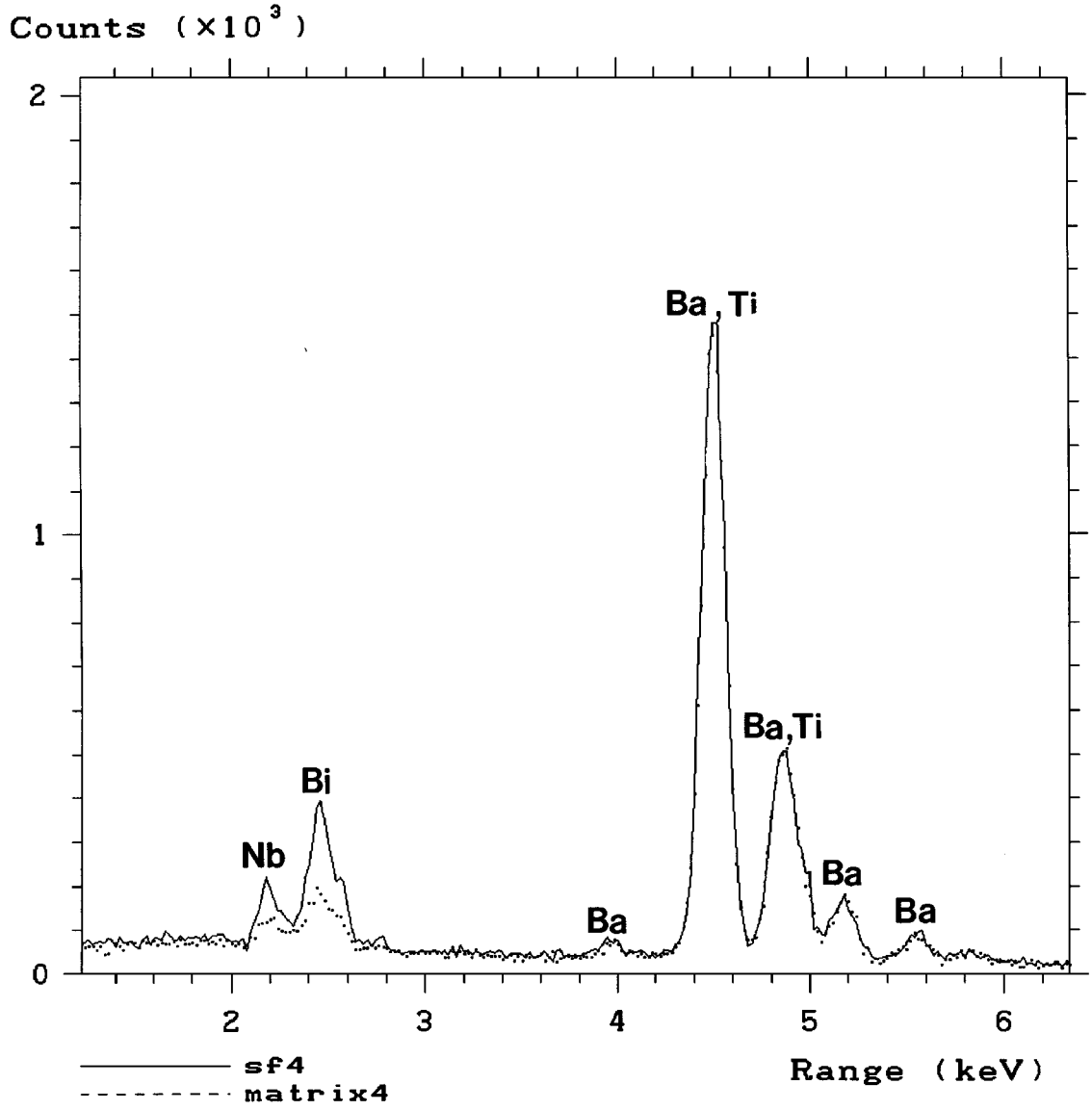

(b)

Figure 5 (*continued*).

TABLE IV Bond distances in stacking fault model and prototype structures

	Bond Distance (nm)*			
Bond	Perovskite†	Bismuth Titanate‡	Unrelaxed Model	Relaxed Model
Ba-O	0.283	—	0.282	0.282
Bi-O	—	0.232	0.199	0.230
		0.292	0.285	0.288
Ti-O	0.195	0.193	0.199	0.199
		0.209		
Ba-Ti	0.343	—	0.346	0.346
Bi-Ba (Ba-Ba)	0.399	—	0.346	0.369
			0.401	0.404

*Nearest-neighbour distances.
†Based on cell parameters ($a = 0.40166$ nm) from Chiang [1] 1988 and the present study.
‡JCPDS card # 35-0795.

3.5. Formation mechanism of planar defects

Twins are readily seen in both doped and undoped $BaTiO_3$ and appear to form as growth defects, primarily under reducing conditions [7]; (1 1 1) twins were also found in calcined powder particles in both Nb-doped and undoped $BaTiO_3$ [13], suggesting that they may pre-exist in the starting powder and persist during subsequent grain growth. Since the twins bisect both the core and the shell, the twins probably existed within the starting $BaTiO_3$ powder particles and persisted as the grains grew during sintering.

Unlike twin boundaries, the formation of stacking faults in $BaTiO_3$ does appear to be controlled by the presence of impurities, primarily codoping of bismuth and niobium. The evidence for this is that (1) they are only observed in the dopant-rich shell region and (2) no reports of stacking faults in undoped $BaTiO_3$ have been found in the literature.

It is interesting to ask why stacking faults are not observed in undoped barium titanate. Clearly, stacking faults based on Models 3 through 8 require a change in stoichiometry. In undoped material, therefore, fault formation would require the formation of a high concentration of charge-compensating defects. In Model 1, which only involves a shear, the interface plane is

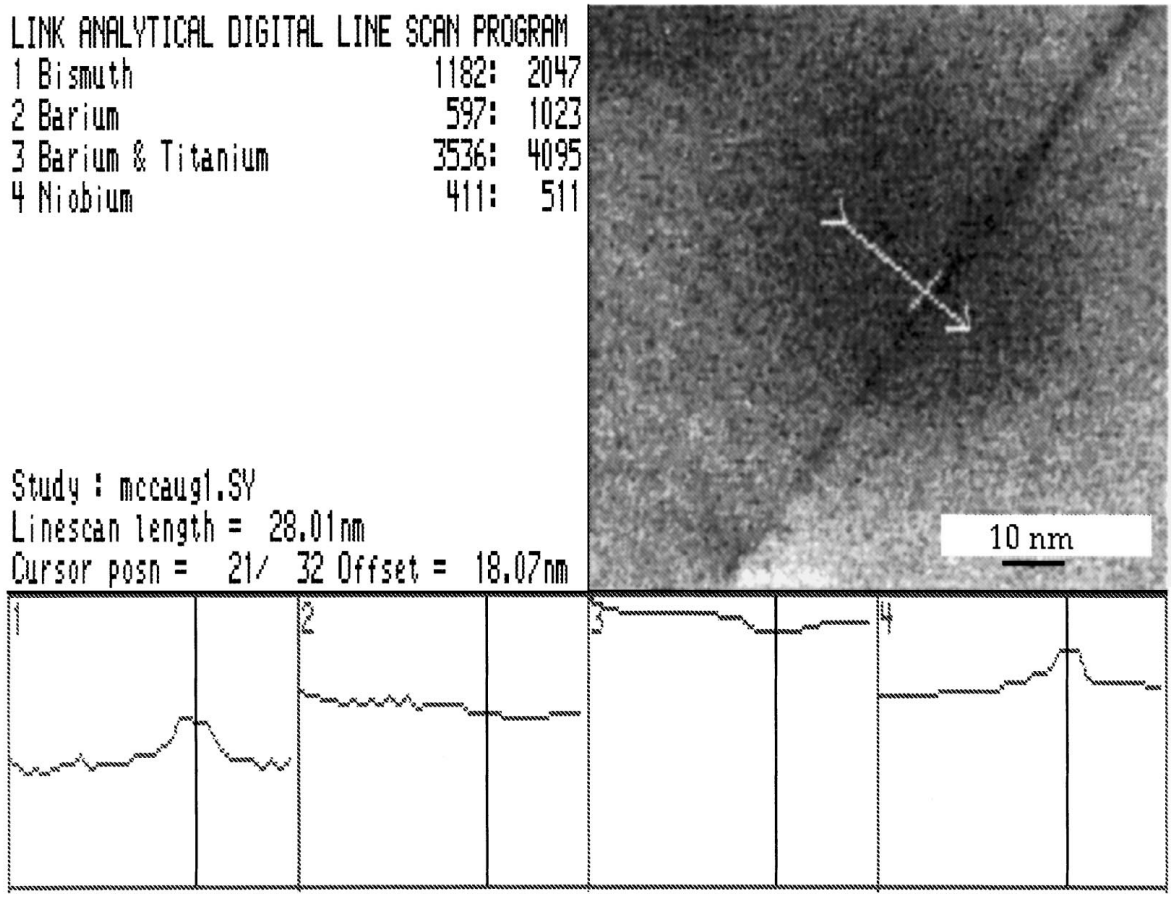

Figure 6 EDS line scans for (1) Bi, (2) Ba, (3) Ti (as determined by Ba+Ti/Ba), and (4) Nb taken across a stacking fault. The position of the fault is noted by the vertical line in the scans. Significantly higher levels of both Nb and Bi are observed within the stacking fault region, as well as an apparent decrease in the Ba+Ti : Ba ratio.

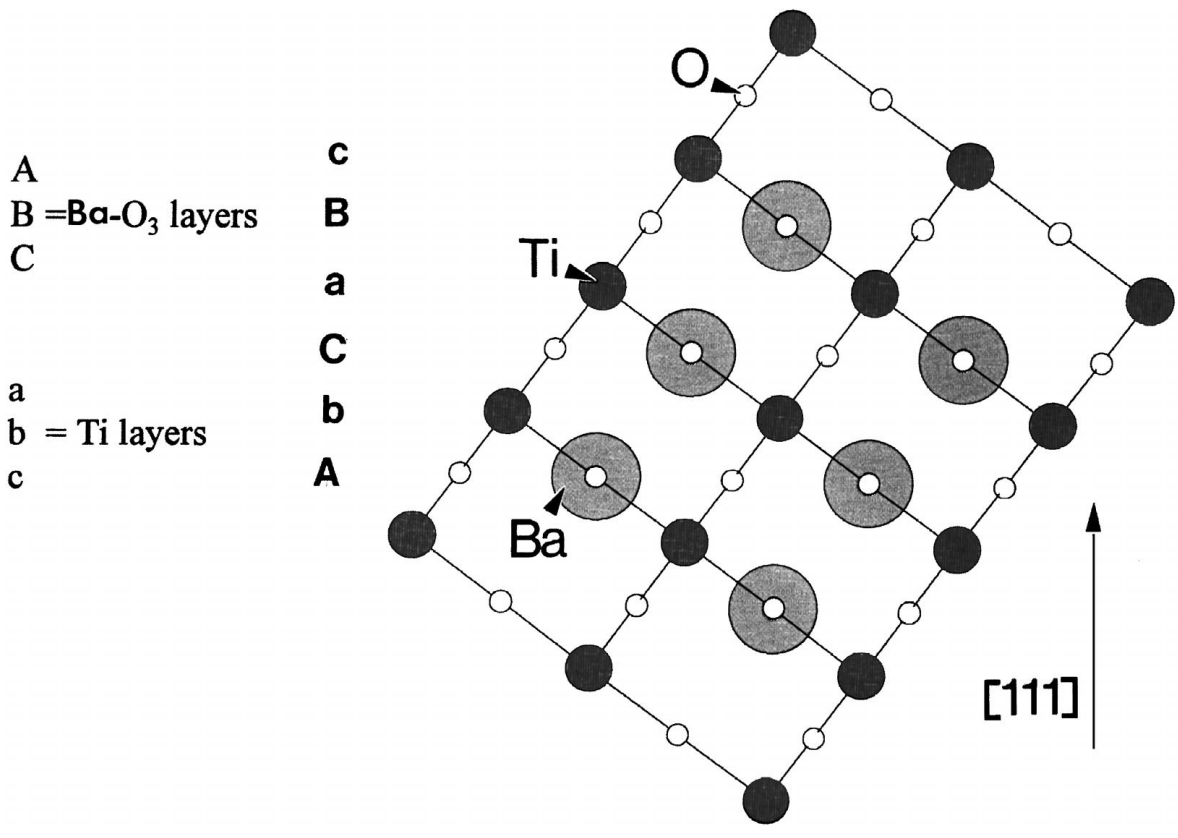

Figure 7 Schematic of $BaTiO_3$ structure projected along $[0\,\bar{1}\,1]$. The structure can be described in terms of alternate stacking of Ba-O_3 layers (denoted by uppercase letters) and Ti layers (denoted by lowercase letters) along [1 1 1] with an interlayer spacing of 1/6[1 1 1]. The repeat unit consists of . . . AbCaBc . . . with a repeat unit of 0.692 nm along [1 1 1].

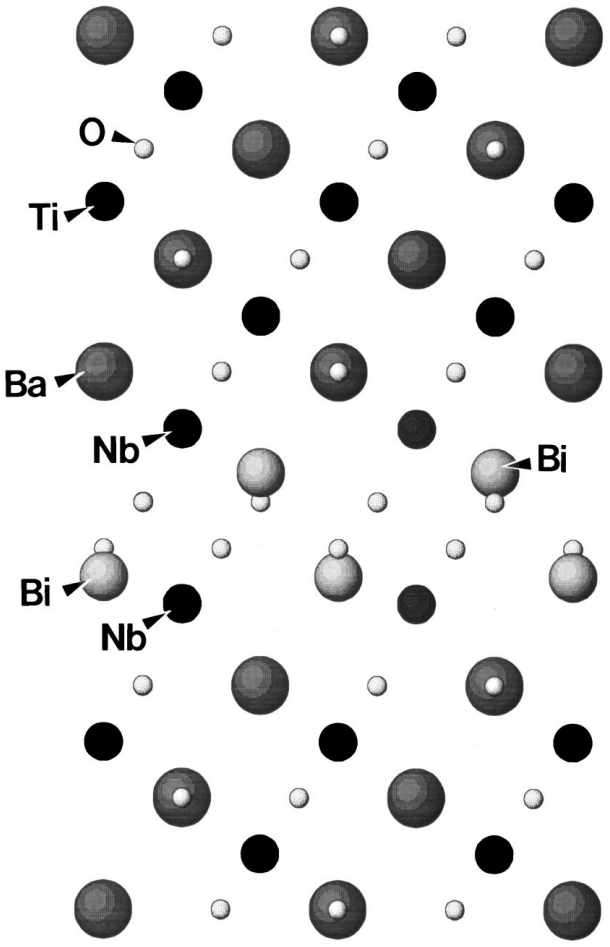

Figure 8 Schematic of stacking fault Model 8 projected along [0 $\bar{1}$ 1], incorporating both a change in stacking sequence and an in-plane shear, with substitution of Bi^{3+} for Ba^{2+} along the interface and of Nb^{5+} in adjacent Ti^{4+} sites. The model includes the rigid body translation measured from the HREM micrographs as well as a slight translation of Bi^{3+} ions (*ca.* 0.05 nm along [1 1 1]).

composed of a titanium layer in a prism-type oxygen co-ordination (*i.e.*, . . .C**b**C. . . in our nomenclature). Based on a previous examination of the structure of (1 1 1) twins in $BaTiO_3$, this configuration is energetically unfavourable [14] compared with a Ba–O_3 interfacial layer, (*i.e.*, . . . a**B**a . . .). This hypothesis was subsequently confirmed in a detailed HREM structural analysis [7].

At least two possible formation mechanisms can be proposed for dopant-induced stacking fault formation. In the first mechanism, the faults nucleate as dislocation loops within the $BaTiO_3$ grain, presumably during cooling, and act as a Bi and Nb sink for a supersaturated solid solution. As the dopant-rich faults grow on {1 1 1} planes, they would deplete the surrounding matrix in Bi and Nb. This mechanism, however, is not consistent with EDS line scans, which showed no depletion zone in the vicinity of the faults.

In the second formation mechanism, the faults form as growth defects during sintering. The growth defects can form either during solid-state sintering or by vapour-phase or liquid-phase assisted growth. The grains may grow either into other $BaTiO_3$ grains or into Bi- and Nb-rich compounds that form early in the sintering process [3]. As the growing grain encounters a dopant-rich phase, the sudden increase in dopant concentration may be accommodated by the formation of a stacking fault. Alternatively, since bismuth oxide has a relatively high vapour pressure at the sintering temperature, a thin Bi-rich layer may condense on the $BaTiO_3$ powder particles from a vapour phase. Barium titanate is reported to form cubo-octahedral morphologies [15] during sintering with faceting along {1 0 0} and {1 1 1} planes; bismuth-rich compounds may form on (1 1 1) $BaTiO_3$ facets and act as a growth defect for subsequent growth of $BaTiO_3$. A similar model has been proposed as a formation mechanism for inversion domain boundaries in Sb-doped ZnO varistors [16]. The condensation mechanism appears unlikely, however, since both Bi and Nb are associated with the defects.

The stacking faults are metastable structures that disappear upon annealing [1], presumably as more bismuth and niobium diffuse from the shell into the core region.

3.6. Point defect chemistry of Bi- and Nb-doped $BaTiO_3$

Both the EDS spot analyses and line scans suggest that Ba : Ti ratio is a function of the dopant concentration, increasing with increasing Bi and Nb concentration. These results suggest that both Bi^{3+} and Nb^{5+} substitute on Ti^{4+} sites. Although the Ti site substitution by niobium has been examined in detail [17], bismuth substitution has been less thoroughly characterized. Because of its relatively high ionic radius (0.102 nm for six fold co-ordination) compared with Ti^{4+} (0.06 nm) [18], Bi^{3+} is generally thought to substitute for Ba^{2+} (ionic radius 0.16 nm) [1] and is observed in dodecahedral sites in Aurivillius phases such as $Bi_4Ti_3O_{12}$ [19]. Thus, the substitution of Bi^{3+} on Ti sites would seem unlikely. There are, however, a number of compounds with the perovskite structure in which Bi^{3+} assumes B(Ti)-site occupancy; in these compounds, B sites are occupied by both 3+ and 5+ cations, for example, $Ba(Bi_{0.5}Nb_{0.5})O_3$ [20]. In general, if the ionic radii of the 3+ and 5+ cations are different, there is a tendency toward Ti-site ordering. The $Ba(Bi_{0.5}Nb_{0.5})O_3$ compound, for example, adopts the cubic $(NH_4)FeF_6$ structure (space group Fm3m, a = 0.863 nm) [21] in which the Ti-site ordering causes a doubling of the perovskite unit cell.

The Ti-site preference of both bismuth and niobium in the codoped material may arise from Bi^{3+} and Nb^{5+} acting as self-compensating defects. Since the solution energy of an aliovalent dopant depends on both the effective ionic radius of the dopant and the energy associated with the formation of charge-compensating defects, the energy associated with the substitution of a larger cation such as Bi^{3+} may be mitigated, since no charge-compensating cation vacancies need be created. In addition, the relatively high dopant concentrations (*ca.* 3–4 atom %) may also lead to defect–defect interactions such as local ordering processes that may further lower the solution energy.

Presumably, without the presence of Nb^{5+}, Bi^{3+} would preferentially occupy the dodecahedral Ba sites,

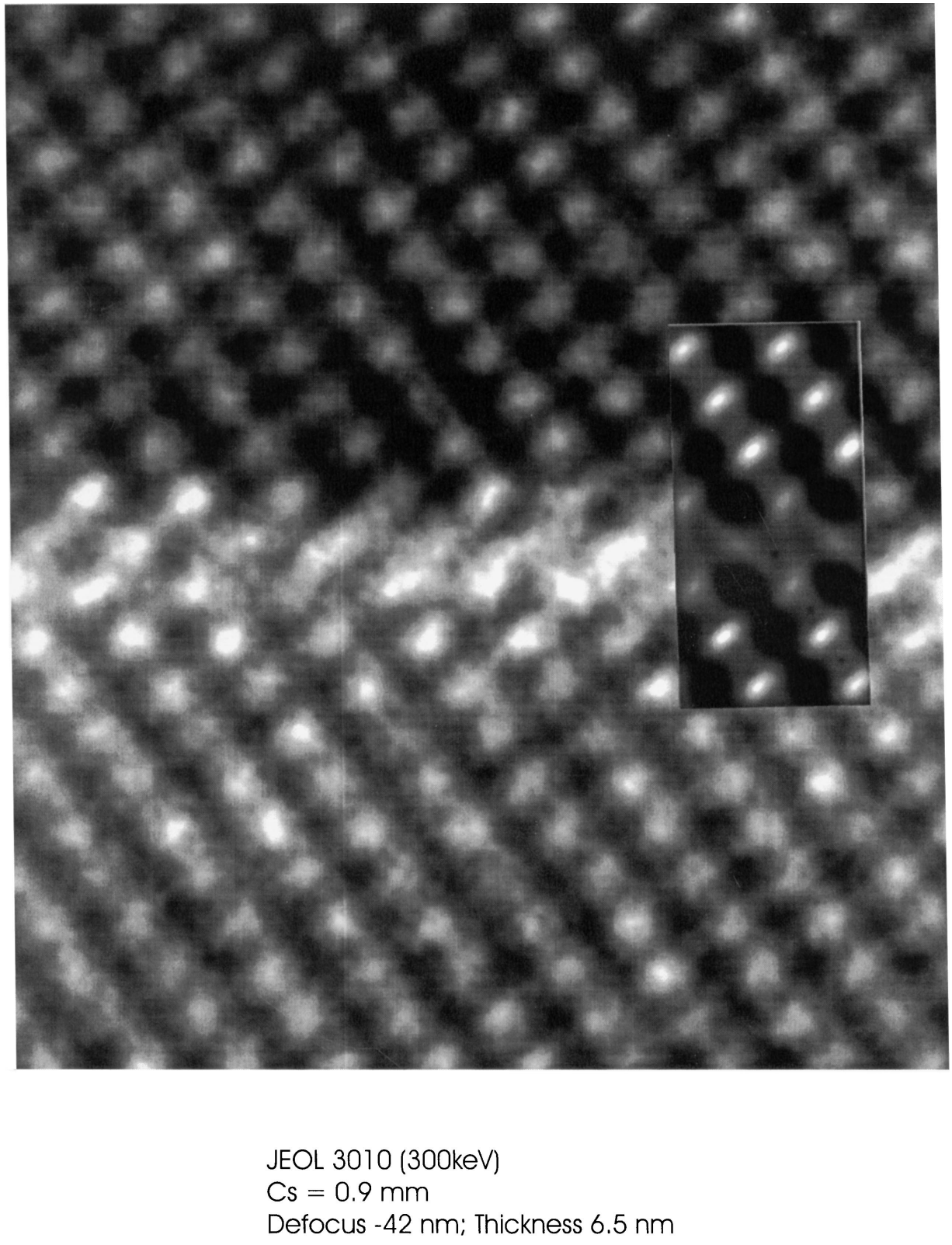

Figure 9 Comparison of HREM and simulated image (inset) based on structural model shown in Fig. 8. The contrast within the interface region in the micrograph contains a high level of disorder, possibly due to complex barium (bismuth) site relaxation.

as observed in Aurivillius-type phases and as was predicted for a number of trivalent impurities with similar ionic radii [22].

4. Summary

Both twins and stacking faults were observed in Nb_2O_5- and Bi_2O_3-doped $BaTiO_3$ lying along {1 1 1} planes. The proposed stacking fault structure, which is consistent with CTEM and HREM observations, consists of a double BiO_3^{3-} layer with substitution of adjacent Ti sites by Nb^{5+} cations. EDS analysis on codoped regions suggest that both bismuth and niobium exhibit a preference for Ti-site occupancy; the driving force for the site preference is the corresponding solution energy decrease afforded by a self-compensation mechanism.

Acknowledgments

The authors acknowledge Rick Ubic (University of Sheffield) for preparation of the ceramic samples and Dr. Ian Reaney (University of Sheffield) for helpful discussions. This work was funded in part by an EPSRC grant (grant number GR/J31629).

References

1. S.-K. CHIANG, Ph.D. Dissertation, Ohio State University, Columbus, OH (1988).
2. S. PATHUMARAK, M. AL-KHAFAJI and W. E. LEE, *Brit. Ceram. Trans.* **93** (1994) 114.
3. S. PATHUMARAK and W. E. LEE, *J. Mater. Sci.: Mater. Electr.* **7** (1996) 161.
4. R. ALSAFFAR, F. AZOUGH and R. FREER, *Inst. Phys. Conf. Ser.* **130** (1993) 379.
5. Y. PARK and Y. KIM, *J. Mater. Res.* **10** (1995) 2770.
6. E. A. D. WHITE, *Acta Cryst.* **8** (1955) 845.
7. A. RECNIK, J. BRULEY, W. MADER, D. KOLAR and M. RUHLE, *Phil. Mag. B,* **70** (1994) 1021.
8. W. E. LEE, I. M. REANEY and M. A. MCCOY, *Brit. Ceram. Proc.* **55** (1996) 199.
9. S. AMELINCKX, in Materials Science and Technology—A Comprehensive Treatment," Vol 2A, edited by R. W. Cahn, P. Haasen and E. J. Kramer (VCH, Weinheim, Germany, 1993) pp. 40–48.
10. P. STADELMANN, *Ultramicroscopy* **21** (1987) 131.
11. Z. AKHTAR, M. AKHTAR and C. R. A. CATLOW, *J. Mater. Chem.* **4** (1994) 1081.
12. R. W. G. WYCKOFF "Crystal Structures," Vol. 3. 2nd ed. (Interscience, London, 1969) p. 488.
13. O. EIBL, P. PONGRATZ, P. SKALICKY and H. SCHMELZ, *J. Am. Ceram. Soc.* **70** (1987) 195.
14. O. EIBL, P. PONGRATZ and P. SKALICKY, *Phil. Mag. B* **57** (1988) 521.
15. G. KASTNER, R. WAGNER and V. HILARIUS, *Phil. Mag. A* **69** (1994) 1051.
16. M. A. MCCOY, W. E. LEE and R. W. GRIMES, *J. Mater. Res.* **11** (1996) 2009.
17. H. CHAN, M. P. HARMER and D. M. SMYTH, *J. Am. Ceram. Soc.* **6** (1986) 507.
18. R. D. SHANNON and C. T. PREWITT, *Acta Cryst.* **B25** (1969) 925; **B26** (1969) 1046.
19. B. AURIVILLIUS, *Arkiv Kemi* **1** (1949) 463.
20. F. S. GALASSO, "Structure, Properties and Preparation of Perovskite-Type Compounds" (Pergamon, Oxford, 1969) pp. 15–27.
21. L. PAULING, *J. Am. Chem. Soc.* **46** (1924) 2738.
22. G. V. LEWIS and C. R. A. CATLOW, *J. Phys. Chem. Solids* **47** (1986) 89.

Received 22 January
and accepted 29 July 1998